

Chapter 5 : Calculating Strain from Displacement

In this chapter, theory and techniques necessary to create strain tensor images from displacement images are described with attention paid towards issues relevant to strain imaging of the carotid artery with external ultrasound. First, the definition of the strain tensor in continuum mechanics and the physical explanation that follows is reviewed. The nomenclature as it applies to diagnostic ultrasound strain imaging is covered. Next, a number of methods to estimate the displacement gradient, which is needed to calculate the strain tensor, are presented. Once the strain tensor has been estimated, permutations can be computed that ease interpretation and derived scalar quantities that be used for statistical analysis of plaque vulnerability. Finally, methods to calculate accumulated strain in digital ultrasound strain images over the cardiac cycle are explained.

5.1 The strain tensor

5.1.1 Mechanical model

An *in situ* plaque prior to failure is a continuous, solid-body at a gross level, and solid-body continuum mechanics can be applied. Solid-body continuum mechanics treats a body as a collection of infinitesimal volumes of material. We are concerned with the motion of this collection of infinitesimal volumes over time. This may be rigid body motion, translation and rotation, or deformation of the body.

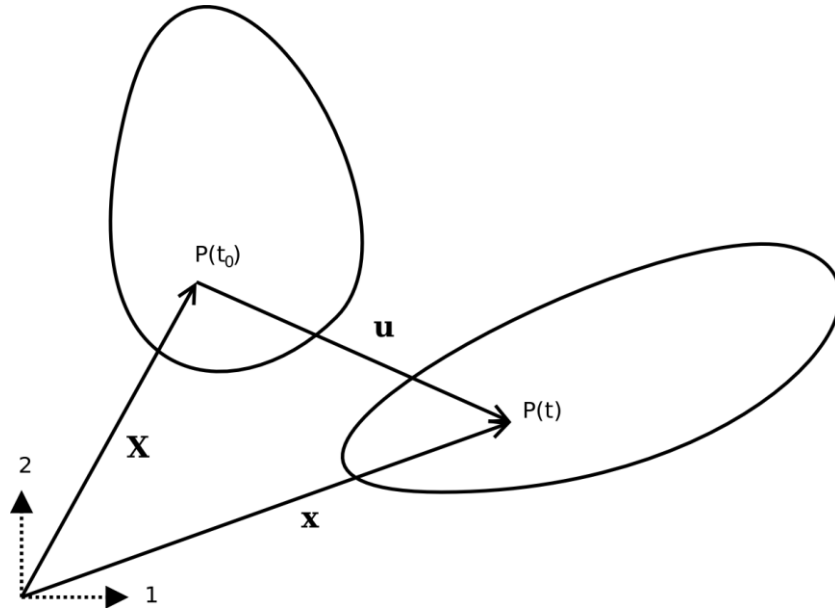


Figure 5.1: 2D solid body at reference time t_0 , and after motion at time t . The vector \mathbf{X} defines the position of point $P(t_0)$ in the reference configuration, and the vector \mathbf{x} defines the point's position after motion. The vector \mathbf{u} is the difference between the two vectors and the displacement of P .

Consider a point, P , within a body at the time t_0 whose location is defined by the vector \mathbf{X} .

Motion occurs and $P(t)$ is now located at \mathbf{x} . That is, $\mathbf{x} = \mathbf{x}(\mathbf{X}, t)$ and $\mathbf{x}(\mathbf{X}, t_0) = \mathbf{X}$. Here \mathbf{X} defines the reference configuration. We will consider the location of P after motion occurs to be the reference location plus a displacement, \mathbf{u} , i.e.

$$\mathbf{x} = \mathbf{X} + \mathbf{u}(\mathbf{X}, t)$$

Eqn. 5.1

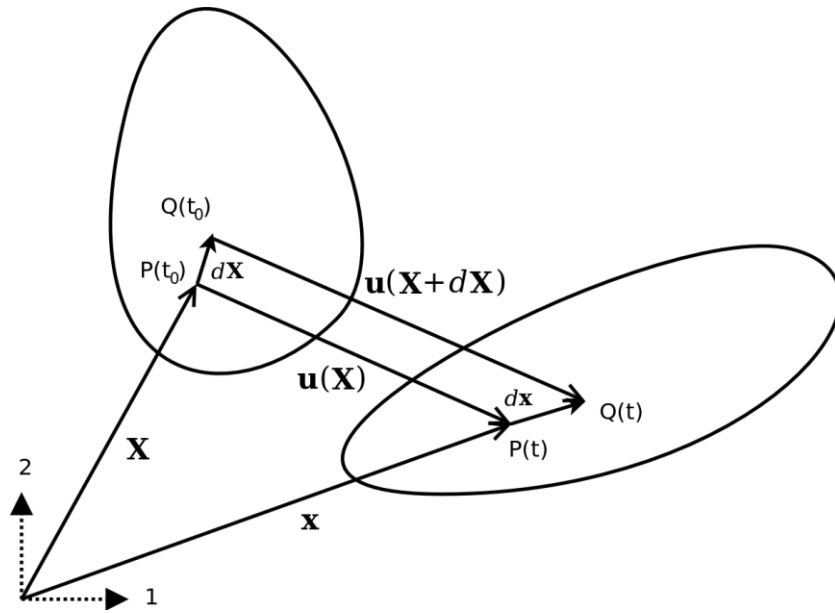


Figure 5.2: A different length segment extending from point P to point Q in the reference configuration, $d\mathbf{X}$, and after deformation, $d\mathbf{x}$.

Let us examine the motion of infinitesimally small line segments within the body. The line segment at \mathbf{X} , $d\mathbf{X}$, at time t becomes $d\mathbf{x}$. This is illustrated in Fig. 5.2. The nearby point Q is located in the post- and pre-deformation states at

$$\mathbf{x} + d\mathbf{x} = \mathbf{X} + d\mathbf{X} + \mathbf{u}(\mathbf{X} + d\mathbf{X}, t)$$

Eqn. 5.2

It is clear from Fig. 5.2 that

$$d\mathbf{x} = d\mathbf{X} + \mathbf{u}(\mathbf{X} + d\mathbf{X}, t) - \mathbf{u}(\mathbf{X}, t)$$

Eqn. 5.3

This can be expressed with the second-order tensor called the displacement gradient [1], $\nabla \mathbf{u}$. In

2D Cartesian coordinates:

$$\nabla \mathbf{u} = \begin{bmatrix} \frac{\partial u_1}{\partial X_1} & \frac{\partial u_1}{\partial X_2} \\ \frac{\partial u_2}{\partial X_1} & \frac{\partial u_2}{\partial X_2} \end{bmatrix}$$

Eqn. 5.4

If \mathbf{F} , the *deformation gradient* [1] is defined by $\mathbf{F} \equiv I + \nabla \mathbf{u}$, then

$$d\mathbf{x} = d\mathbf{X} + \nabla \mathbf{u} d\mathbf{X} = \mathbf{F} d\mathbf{X}$$

Strain, which quantifies the distortion that occurs in a material, is defined when investigating the expression for the inner product between two differential segments before and after deformation. When we compare the two segments $d\mathbf{x}^{(1)}$ and $d\mathbf{x}^{(2)}$

$$\begin{aligned} d\mathbf{x}^{(1)} \cdot d\mathbf{x}^{(2)} &= \mathbf{F} d\mathbf{X}^{(1)} \cdot \mathbf{F} d\mathbf{X}^{(2)} \\ &= d\mathbf{X}^{(1)} \cdot \mathbf{F}^T \mathbf{F} d\mathbf{X}^{(2)} \end{aligned}$$

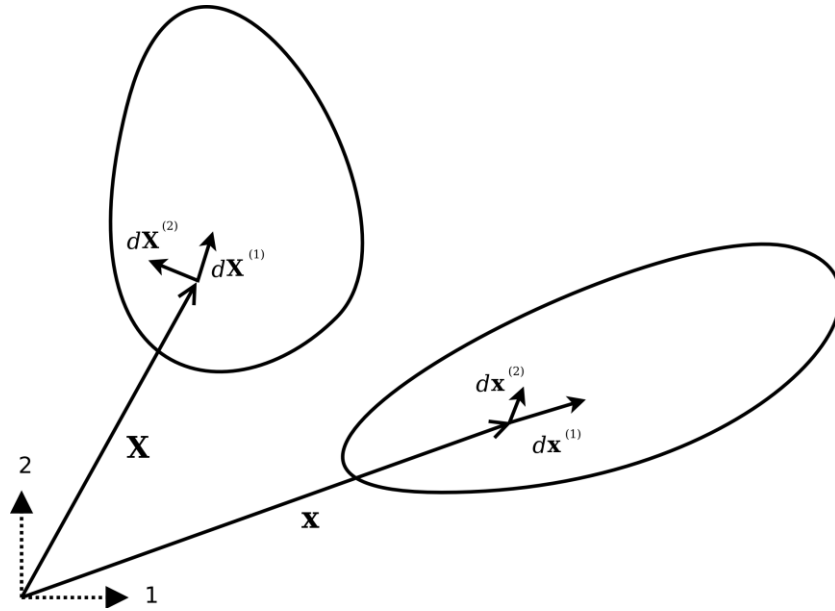


Figure 5.3: Two differential segments in the reference configuration, $d\mathbf{x}^{(1)}$ and $d\mathbf{x}^{(2)}$, and after motion occurs. $d\mathbf{X}^{(1)}$ and $d\mathbf{X}^{(2)}$

Observe that

$$\begin{aligned}\mathbf{F}^T \mathbf{F} &= (\mathbf{I} + \nabla \mathbf{u})^T (\mathbf{I} + \nabla \mathbf{u}) \\ &= \mathbf{I} + \nabla \mathbf{u} + (\nabla \mathbf{u})^T + (\nabla \mathbf{u})^T \nabla \mathbf{u}\end{aligned}$$

Eqn. 5.5

It is from this model that the different expressions for the strain tensor arise.

5.1.1.1 Infinitesimal strain

If there are very small deformations, $(\nabla \mathbf{u})^T \nabla \mathbf{u}$ becomes negligible, and

$$\mathbf{F}^T \mathbf{F} \approx \mathbf{I} + \nabla \mathbf{u} + (\nabla \mathbf{u})^T \equiv \mathbf{I} + 2\mathbf{E}$$

Eqn. 5.6

where

$$\mathbf{E} = \frac{1}{2}((\nabla \mathbf{u})^T + \nabla \mathbf{u})$$

Eqn. 5.7

Note that \mathbf{E} is a second-rank tensor since $\nabla \mathbf{u}$ is a second-rank tensor, and it is symmetric because we have the transpose added to itself. The tensor \mathbf{E} is the *infinitesimal strain* [1], also known as *engineering strain* or *small strain*. We then have:

$$d\mathbf{x}^{(1)} \cdot d\mathbf{x}^{(2)} = d\mathbf{X}^{(1)} \cdot d\mathbf{X}^{(2)} + 2d\mathbf{X}^{(1)} \cdot \mathbf{E}d\mathbf{X}^{(2)}$$

Eqn. 5.8

Therefore, the change in the inner product is an additive term with transformation of the original vectors being performed by the strain tensor.

For Cartesian coordinates in Einstein notation,

$$E_{ij} = \frac{1}{2} \left(\frac{\partial u_i}{\partial X_j} + \frac{\partial u_j}{\partial X_i} \right)$$

Eqn. 5.9

and in 2D the infinitesimal strain tensor is explicitly defined as,

$$\mathbf{E} = \begin{bmatrix} \frac{\partial u_1}{\partial X_1} & \frac{1}{2}(\frac{\partial u_1}{\partial X_2} + \frac{\partial u_2}{\partial X_1}) \\ \frac{1}{2}(\frac{\partial u_1}{\partial X_2} + \frac{\partial u_2}{\partial X_1}) & \frac{\partial u_2}{\partial X_2} \end{bmatrix}$$

Eqn. 5.10

We can elucidate the physical meaning of the infinitesimal strain tensor by examining special cases for $d\mathbf{X}^{(1)}$ and $d\mathbf{X}^{(2)}$. First, let us consider when $d\mathbf{X}^{(1)} = d\mathbf{X}^{(2)} = dS \mathbf{e}_1$ where \mathbf{e}_1 is the unit basis in direction 1 and dS is the length of $d\mathbf{X}$, and ds is the deformed length of $d\mathbf{x}^{(1)} = d\mathbf{x}^{(2)}$.

$$\begin{aligned} ds^2 &= dS^2 + 2dS \mathbf{e}_1 \cdot \mathbf{E} dS \mathbf{e}_1 \\ (ds)^2 - (dS)^2 &= 2(dS)^2 \mathbf{e}_1 \cdot \mathbf{E} \mathbf{e}_1 \\ (ds + dS)(ds - dS) &= 2(dS)^2 \mathbf{e}_1 \cdot \mathbf{E} \mathbf{e}_1 \end{aligned}$$

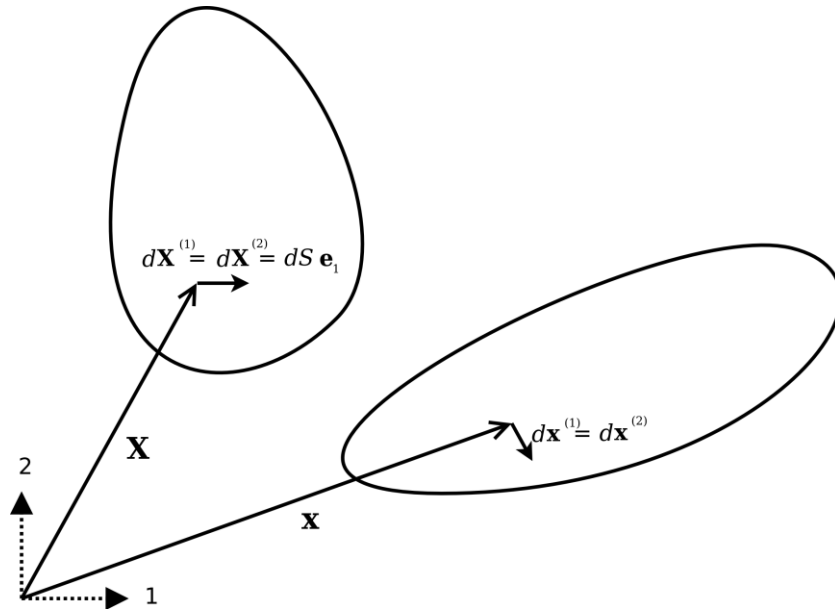


Figure 5.4: Two line segments, $d\mathbf{X}^{(1)} = d\mathbf{X}^{(2)} = dS \mathbf{e}_1$ get transformed to a segment of length ds after deformation.

For small deformations, $(ds + dS)(ds - dS) \approx 2dS(ds - dS)$, and

$$\frac{ds - dS}{dS} = \mathbf{e}_1 \cdot \mathbf{E} \mathbf{e}_1 = E_{11}$$

Eqn. 5.11

Therefore, E_{11} is equal to the unit elongation (or shortening) for the segment in the direction of \mathbf{e}_1 . Similarly, E_{22} is the unit elongation for the segment that is in the direction of \mathbf{e}_2 . These diagonal elements of \mathbf{E} constitute the *normal strains* [1]. Note that

$$100 \frac{ds - dS}{dS} \equiv \% \text{ elongation of } dS$$

Eqn. 5.12

Therefore, in the small strain case, a normal strain component multiplied by 100 is equal to the percent elongation. A positive normal strain indicates an extension of dS , and a negative normal strain indicates a shortening of dS .

Secondly, instead of examining parallel segments centered at \mathbf{X} , let us investigate perpendicular segments.

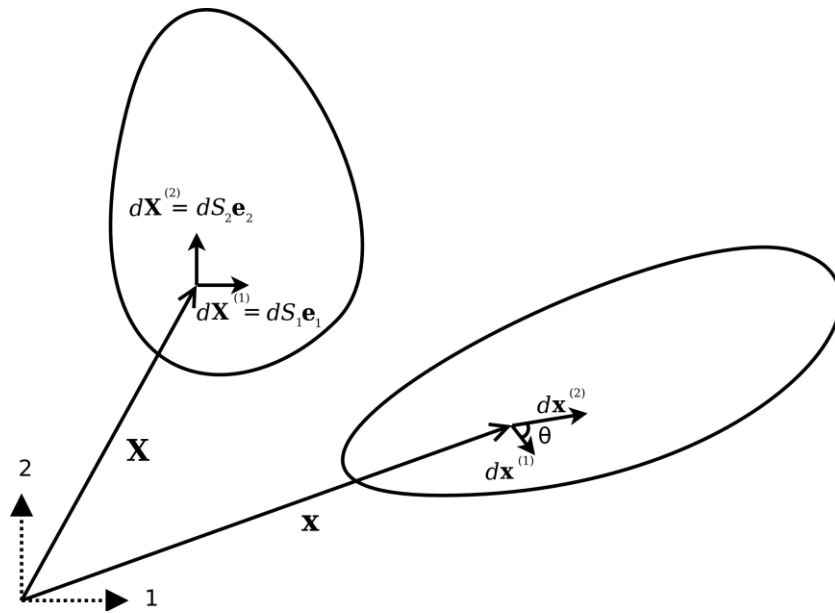


Figure 5.5: Relative change that occurs, which is orthogonal in the reference configuration.

Let $d\mathbf{X}^{(1)} = dS_1 \mathbf{e}_1$ and $d\mathbf{X}^{(2)} = dS_2 \mathbf{e}_2$, $\|d\mathbf{x}^{(1)}\| = ds_1$, $\|d\mathbf{x}^{(2)}\| = ds_2$, and the angle between $\mathbf{x}^{(1)}$ and $\mathbf{x}^{(2)}$ is θ .

$$\begin{aligned} ds_1 ds_2 \cos \theta &= 2dS_1 dS_2 \mathbf{e}_1 \cdot \mathbf{E}\mathbf{e}_2 \\ \cos \theta &= 2 \frac{dS_1}{ds_1} \frac{dS_2}{ds_2} E_{12} \end{aligned}$$

If we define $\theta = \pi/2 - \gamma$, then γ is the change in angle that occurs between $\mathbf{x}^{(1)}$ and $\mathbf{x}^{(2)}$.

$$\sin \gamma = \cos(\pi/2 - \gamma)$$

Eqn. 5.12

For small strain

$$\sin \gamma \approx \gamma, \quad \frac{dS_1}{ds_1} \approx 1, \quad \frac{dS_2}{ds_2} \approx 1$$

Eqn. 5.13

$$\gamma = 2 E_{12} = 2 E_{21}$$

Eqn. 5.14

That is, for infinitesimal strain, the decrease in angle between orthogonal segments is equal to twice the diagonal component of the strain tensor, the *shear strain* [1].

5.1.1.2 Lagrangian strain

Beginning again without presuming there are very small deformations, we start at Fig. 5.3 and subtract $d\mathbf{X}^{(1)} \cdot d\mathbf{X}^{(2)}$ from both sides of the equation:

$$\begin{aligned} d\mathbf{x}^{(1)} \cdot d\mathbf{x}^{(2)} - d\mathbf{X}^{(1)} \cdot d\mathbf{X}^{(2)} &= d\mathbf{X}^{(1)} \cdot \mathbf{F}^T \mathbf{F} d\mathbf{X}^{(2)} - d\mathbf{X}^{(1)} \cdot d\mathbf{X}^{(2)} \\ &= d\mathbf{X}^{(1)} \cdot (\mathbf{F}^T \mathbf{F} - \mathbf{I}) d\mathbf{X}^{(2)} \\ &= 2\mathbf{X}^{(1)} \cdot \mathbf{E}^* d\mathbf{X}^{(2)} \end{aligned}$$

Eqn. 5.15

where $\mathbf{E}^* = \frac{1}{2}(\mathbf{F}^T \mathbf{F} - \mathbf{I})$ is the *Green-Lagrangian strain tensor* [1, 2]. This is a finite strain

tensor that specifies strain in terms of the reference configuration.

Again examining the situation in Fig. 5.4, where $d\mathbf{X}^{(1)} = d\mathbf{X}^{(2)} = d\mathbf{X} = dS\mathbf{e}_1$ and $\|d\mathbf{x}\| = ds$,

$$ds^2 - dS^2 = 2dS\mathbf{e}_1 \cdot \mathbf{E}^* dS\mathbf{e}_1$$

$$E_{11}^* = \frac{ds^2 - dS^2}{2dS^2}$$

Eqn. 5.16

Similarly, if $d\mathbf{X} = dS\mathbf{e}_2$,

$$E_{22}^* = \frac{ds^2 - dS^2}{2dS^2}$$

Eqn. 5.17

And, if we again look at Fig. 5.5, where $d\mathbf{X}^{(1)} = ds_1\mathbf{e}_1$ and $d\mathbf{X}^{(2)} = dS_2\mathbf{e}_2$ deform to $d\mathbf{x}^{(1)} = ds_1\mathbf{m}$ and $d\mathbf{x}^{(2)} = ds_2\mathbf{n}$ where \mathbf{m} and \mathbf{n} are unit vectors,

$$ds_1 ds_2 \mathbf{m} \cdot \mathbf{n} = 2dS_1 dS_2 \mathbf{e}_1 \cdot \mathbf{E}^* \mathbf{e}_2$$

Eqn. 5.18

$$E_{12}^* = \frac{ds_1 ds_2}{2dS_1 dS_2} \cos(\mathbf{m}, \mathbf{n})$$

Eqn. 5.19

The expression of \mathbf{E}^* in terms of the displacement gradient is

$$\mathbf{E}^* = \frac{1}{2}(\nabla \mathbf{u} + (\nabla \mathbf{u})^T + (\nabla \mathbf{u})^T \nabla \mathbf{u})$$

Eqn. 5.20

In Einstein summation notation,

$$E_{ij}^* = \frac{1}{2} \left(\frac{\partial u_i}{\partial X_i} + \frac{\partial u_j}{\partial X_i} + \frac{1}{2} \frac{\partial u_m}{\partial X_i} \frac{\partial u_m}{\partial X_j} \right)$$

Eqn. 5.21

The explicit components in a 2D Cartesian coordinate system are,

$$\begin{aligned} E_{11}^* &= \frac{\partial u_1}{\partial X_1} + \frac{1}{2} \left(\left(\frac{\partial u_1}{\partial X_1} \right)^2 + \left(\frac{\partial u_2}{\partial X_1} \right)^2 \right) \\ E_{12}^* &= \frac{1}{2} \left(\frac{\partial u_1}{\partial X_2} + \frac{\partial u_2}{\partial X_1} \right) + \frac{1}{2} \left(\frac{\partial u_1}{\partial X_1} \frac{\partial u_1}{\partial X_2} + \frac{\partial u_2}{\partial X_1} \frac{\partial u_2}{\partial X_2} \right) \\ E_{22}^* &= \frac{\partial u_2}{\partial X_2} + \frac{1}{2} \left(\left(\frac{\partial u_1}{\partial X_2} \right)^2 + \left(\frac{\partial u_2}{\partial X_2} \right)^2 \right) \end{aligned}$$

Eqn. 5.22

5.1.1.3 Eulerian strain

Instead of specifying motion in terms of the reference configuration, it can be specified in the deformed configuration,

$$d\mathbf{X} = \mathbf{F}^{-1} d\mathbf{x}$$

Eqn. 5.23

where \mathbf{F}^{-1} is the inverse of \mathbf{F} [1],

$$\mathbf{F}^{-1} = \begin{bmatrix} \frac{\partial X_1}{\partial x_1} & \frac{\partial X_1}{\partial x_2} \\ \frac{\partial X_2}{\partial x_1} & \frac{\partial X_2}{\partial x_2} \end{bmatrix}$$

Eqn. 5.24

Again considering the deformation of two small segments in the volume,

$$\begin{aligned} d\mathbf{X}^{(1)} \cdot d\mathbf{X}^{(2)} &= \mathbf{F}^{-1} d\mathbf{x}^{(1)} \cdot \mathbf{F}^{-1} d\mathbf{x}^{(2)} \\ &= d\mathbf{x}^{(1)} \cdot (\mathbf{F}^{-1})^T \mathbf{F}^{-1} d\mathbf{x}^{(2)} \\ &= d\mathbf{x}^{(1)} \cdot (\mathbf{F}\mathbf{F}^T)^{-1} d\mathbf{x}^{(2)} \end{aligned}$$

Eqn. 5.25

Subtracting the above from $d\mathbf{x}^{(1)} \cdot d\mathbf{x}^{(2)}$ to again obtain an expression for the change in the inner product between the two segments,

$$\begin{aligned} d\mathbf{x}^{(1)} \cdot d\mathbf{x}^{(2)} - d\mathbf{X}^{(1)} \cdot d\mathbf{X}^{(2)} &= d\mathbf{x}^{(1)} \cdot d\mathbf{x}^{(2)} - d\mathbf{x}^{(1)} \cdot (\mathbf{F}\mathbf{F}^T)^{-1} d\mathbf{x}^{(2)} \\ &= d\mathbf{x}^{(1)} \cdot (\mathbf{I} - (\mathbf{F}\mathbf{F}^T)^{-1}) d\mathbf{x}^{(2)} \\ &= 2 d\mathbf{x}^{(1)} \cdot \mathbf{e}^* d\mathbf{x}^{(2)} \end{aligned}$$

Eqn. 5.26

where $\mathbf{e}^* = \frac{1}{2}(\mathbf{I} - (\mathbf{F}\mathbf{F}^T)^{-1})$ is the *Eulerian-Almansi strain tensor* [1, 2]. This is a finite strain tensor that specifies strain in terms of the deformed configurations.

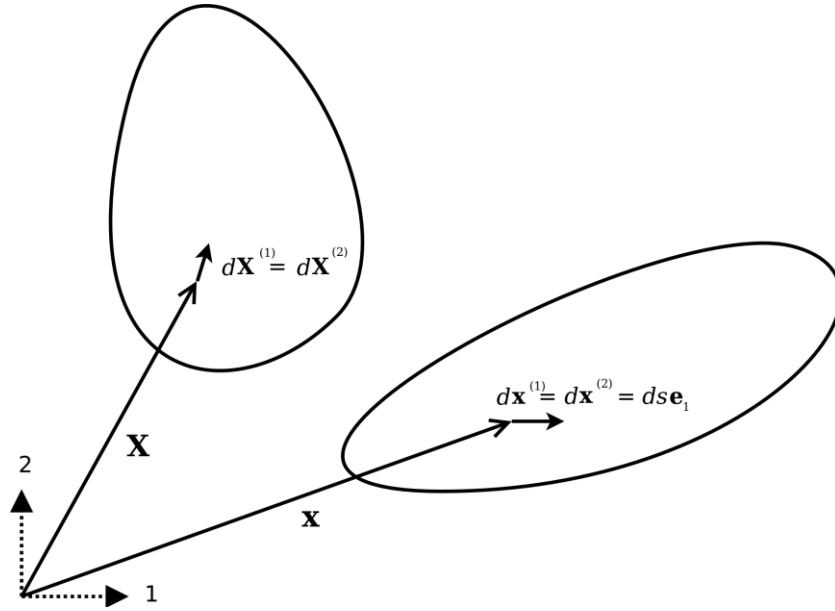


Figure 5.6: Two identical line segments, this time in the deformed configuration, are transformed from a segment of length dS .

As shown in Fig. 5.6, if $dx^{(1)} = dx^{(2)} = dx = ds\mathbf{e}_1$ and $\|dx\| = dS$, then

$$ds^2 - dS^2 = 2ds\mathbf{e}_1\mathbf{e}^*ds\mathbf{e}_1$$

Eqn. 5.27

$$e_{11}^* = \frac{ds^2 - dS^2}{2dS^2}$$

Eqn. 5.28

And, when considering two segments $dx^{(1)} = ds_1\mathbf{e}_1$ and $dx^{(2)} = ds_2\mathbf{e}_2$ that deformed from

$d\mathbf{X}^{(1)} = dS_1 \mathbf{n}$ and $d\mathbf{X}^{(2)} = dS_2 \mathbf{m}$ where \mathbf{n} and \mathbf{m} are unit vectors,

$$-dS_1 dS_2 \mathbf{n} \cdot \mathbf{m} = 2 ds_1 ds_2 \mathbf{e}_1 \cdot \mathbf{e}^* \mathbf{e}_2$$

Eqn. 5.29

$$e_{12}^* = \frac{-dS_1 dS_2 \cos(\mathbf{n}, \mathbf{m})}{2ds_1 ds_2}$$

Eqn. 5.30

Since $\mathbf{F}^{-1} = \mathbf{I} - \nabla_x \mathbf{u}$ [1] (∇_x indicates differentiation with respect to coordinates of the deformed configuration),

$$\begin{aligned} (\mathbf{F}\mathbf{F}^T)^{-1} &= (\mathbf{I} - \nabla_x \mathbf{u})^T (\mathbf{I} - \nabla_x \mathbf{u}) \\ &= \mathbf{I} - \nabla_x \mathbf{u} - (\nabla_x \mathbf{u})^T + (\nabla_x \mathbf{u})^T \nabla_x \mathbf{u} \end{aligned}$$

Eqn. 5.31

and

$$\mathbf{e}^* = \frac{1}{2}(\nabla_x \mathbf{u} + (\nabla_x \mathbf{u})^T - (\nabla_x \mathbf{u})^T \nabla_x \mathbf{u})$$

Eqn. 5.32

In Einstein summation notation,

$$e_{ij}^* = \frac{1}{2} \left(\frac{\partial u_i}{\partial x_i} + \frac{\partial u_j}{\partial x_j} \right) - \frac{1}{2} \frac{\partial u_m}{\partial x_i} \frac{\partial u_m}{\partial x_j}$$

Eqn. 5.33

Explicitly in 2D Cartesian coordinates,

$$\begin{aligned} e_{11}^* &= \frac{\partial u_1}{\partial x_1} - \frac{1}{2} \left(\left(\frac{\partial u_1}{\partial x_1} \right)^2 + \left(\frac{\partial u_2}{\partial x_1} \right)^2 \right) \\ e_{12}^* &= \frac{1}{2} \left(\frac{\partial u_1}{\partial x_2} + \frac{\partial u_2}{\partial x_1} \right) - \frac{1}{2} \left(\frac{\partial u_1}{\partial x_1} \frac{\partial u_1}{\partial x_2} + \frac{\partial u_2}{\partial x_1} \frac{\partial u_2}{\partial x_2} \right) \\ e_{22}^* &= \frac{\partial u_2}{\partial x_2} - \frac{1}{2} \left(\left(\frac{\partial u_1}{\partial x_2} \right)^2 + \left(\frac{\partial u_2}{\partial x_2} \right)^2 \right) \end{aligned}$$

Eqn. 5.34

5.1.2 Application in ultrasound

By applying various medical imaging modalities, strain images of tissues can be created by performing deformable image registration of tissue after deformation to another pre-deformation image. This technique has been applied in multiple imaging modalities. Strain in atherosclerotic tissues was imaged by Rogowska et al. [3, 4] with optical coherence tomography as well as by others [5, 6]. Recently, the high resolutions of X-ray computed tomography (CT) were used to create high quality strain images of a breast phantom [7]. Creation of displacement images in magnetic resonance imaging (MRI) is unique in that does not need to use traditional image registration techniques, but pulse sequences can generate displacement images using the physics of image acquisition [8, 9, 10, 11, 12, 13, 14, 15].

Diagnostic ultrasound has the longest history of calculating strain [16, 17, 18, 19]. In one of

the earliest papers, Ophir et al. [20] calculated strain using:

$$s_i = \frac{t_{i+1} - t_i}{2dz/c}$$

Eqn. 5.35

where the s_i is the local strain, t_{i+1} and t_i are the time shifts of windows on an A-line, dz is the distance between the windows, and c is the speed of sound in tissue. As shown in Fig. 5.7, an A-line, denotes an amplitude line of the radio-frequency (RF) echo-signal created by sending a beam of ultrasound into a tissue. If the speed of sound in tissue is constant, this dimensionless quantity is equivalent to a single component of the infinitesimal strain tensor described in Section 5.1.1.1. Since this component of strain is along the beam axis, it is also called the *axial strain*. In a linear array where all A-lines are acquired along parallel directions, as shown in Fig. 5.7, the term axial refers to the same direction across the entire image. Note that for sector arrays, this may not be the case. In the usual operation and clinical presentation of linear array data, the axial direction is the vertical or depth direction in an image. If beam steering occurs, the beams will remain parallel, but the axial direction no longer corresponds to the vertical direction of the image.

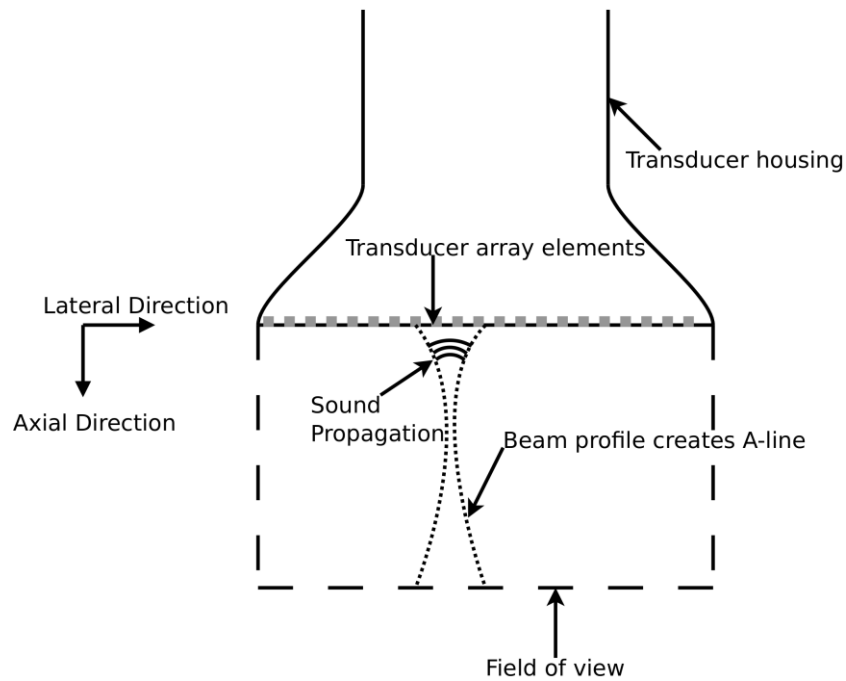


Figure 5.7: Diagram of a medical linear ultrasound array. Small transducer elements on the surface of the handheld transducer send sound concentrated over a beam in the tissue, which creates a line in the image. The axis of this beam determines the *axial direction* of the strain tensor, and the direction orthogonal is the *lateral direction*.

In conventional ultrasound imaging, a B-Mode image is formed by repeatedly changing the location of the ultrasound beam sent into the tissue. In a linear array, the spacing of the A-lines is determined by the transducer element spatial density or pitch. This direction which is orthogonal to the axial direction is the *lateral direction*. In the carotid images shown in this work, the lateral direction corresponds to the horizontal direction in the B-mode image. Resolution in this direction is not directly determined by the excitation frequency as it is in the axial direction, but by the beam width. As a consequence, resolution in this direction is much lower [21]. Also, shifts do not depend on sound speed assumptions; they are statically determined by the geometry of the transducer. In *in vivo* carotid images used in this study, for

example, the number of samples in a 40×40 mm image in the axial direction is 2076 in the axial direction and 244 in the lateral direction. This near ten-fold disparity in the resolution is associated with the difficulty in calculating lateral strains. The majority of the literature has focused on axial strains because the lateral strains do not exhibit a useable signal-to-noise ratio. Only until recently have algorithmic improvements, such as regularization described in Chapter 3 or other improvements described in Chapters 4 and 9, enabled the use of the lateral strain component.

Shear strain in ultrasound strain imaging usually refers to the strain between the axial and lateral directions. Since displacement estimates in the axial direction are of higher quality than those in the lateral directions, some have only calculated the derivative of displacement in the axial direction with respect to the lateral direction and called this *axial shear* [22].

Of course, while axial, lateral, and shear strain provide all components of a 2D strain tensor, physical tissues are 3D. The number of independent components in a symmetric, second-rank tensor is:

$$n_c = D \frac{D + 1}{2}$$

Eqn. 5.36

Note that there are six components in the 3D strain tensor; two additional shear strain components and one additional normal strain component. While there is on-going research to obtain these components, there are a number of technological limitations at this time that prevent full population of the strain tensor with ultrasound. The third direction of a linear array, the *elevational direction*, has a resolution at the level of or worse than the lateral resolution.

Technology to commercially develop a 2D matrix-array of transducer elements is only emerging. Challenges here include creation of the 2D array elements and acquiring the appropriate channel count in the system [23, 24]. In terms of motion tracking, computational challenges exist in terms of data storage and processing. Also, frames rates are slower with volumetric imaging, which in some cases allow too much motion to take place between image sets. However, progress in 3D strain imaging is taking place [25, 26, 27, 28, 29]. Currently, the primary benefit of 3D imaging systems are not necessarily to obtain all components of the strain tensor, but to prevent tissue from moving outside of the imaging plane, which makes motion tracking difficult.

5.2 Methods for estimating strain from displacement

In Section 5.1.1, it was shown how strain tensors are composed of the symmetric part of the displacement gradient. Therefore, in order to compute the strain tensor, the displacement gradient must first be estimated. Accurate calculation of the displacement gradient is a challenge for two reasons. First, the output of block-matching methods is discrete instead of continuous displacement fields. Secondly, displacement estimates are often noisy, and the differential operation of gradient calculation magnifies the noise. In this section, a number of methods to compute the displacement gradient are examined.

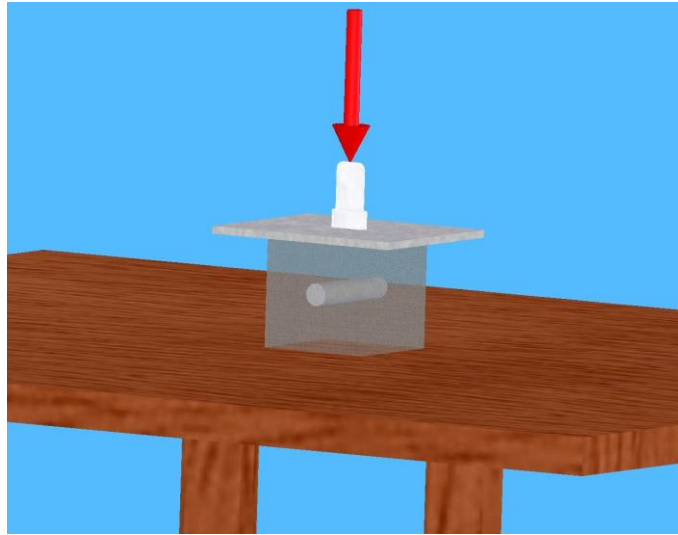


Figure 5.8: Illustration of the mechanical model from which the displacements and strains in this chapter are studied. A block with homogeneous stiffness has a stiffer cylindrical inclusion embedded within. The block is compressed uniaxially with a plate and pre- and post-deformation images are made of the transverse plane of the cylinder with a transducer placed at the top of the assembly.

A common test case for ultrasound strain imaging is the model of a stiffer cylindrical inclusion (high elastic modulus) embedded in a soft background (low elastic modulus). The inclusion exists in a cubic block, and is subject to uniform compression from the top while being unconstrained at the side (zero-traction stress boundary conditions), as shown in Fig. 5.8. Displacement is assumed to start from zero at the top and center of the model as if an ultrasound transducer exists there as a point of reference. Details on methods to create the mechanical finite element and ultrasound scattering parts of a simulation that represents this model are described in Chapter 3. In this section, images resulting from a 3% compression along the axis of deformation in this model will be used to evaluate the behavior of different methods to calculate the strain tensor from tracked displacement vectors.

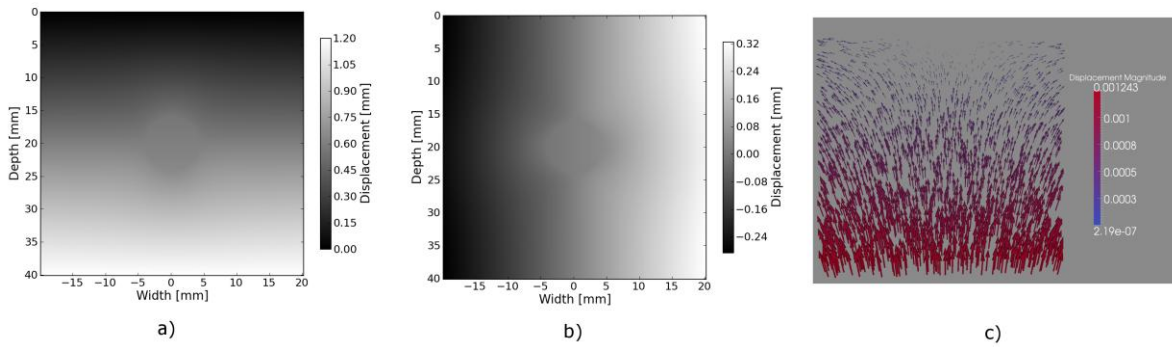


Figure 5.9: Ideal input displacements resulting from the mechanical model. a) Axial displacements, b) lateral displacements, c) displacement vectors represented by arrows scaled and colored by their magnitude.

The ideal, known displacements are shown in Fig. 5.9. Axial displacements start from zero at the transducer surface and increase further into the phantom. Lateral displacements are assumed to be zero along the center axis of the transducer and diverge to the edges of the phantom.

If we apply the central difference methods and the equations in Section 5.1.1.1 to the noiseless known input displacements, Fig. 5.9, we obtain the expected strains in Fig. 5.10.

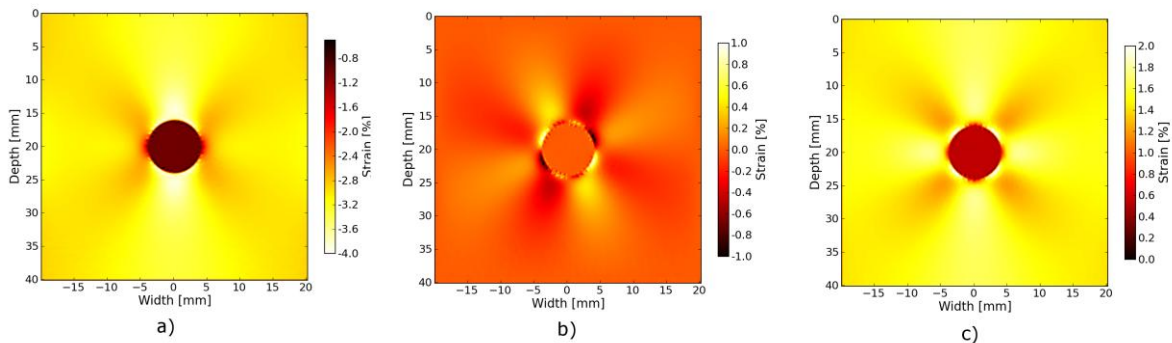


Figure 5.10: Strains calculated from the noiseless input displacements on a hard cylindrical input model undergoing uni-axial compression. a) Axial strain, b) shear strain, and c) lateral strain.

The challenge arises when noise in the displacements are present from imperfect motion tracking. RF ultrasound simulation images in Fig. 5.11 display image content before and after deformation. The deformation pattern that takes place between these images is not readily apparent, but the motion tracking algorithm is able to determine the movement of regions in the image. Notice the anisotropy in resolution-- signal content is much higher in the axial direction than it is in the lateral direction. This leads to higher quality motion estimation in the axial direction, as discussed in Section 5.1.2.

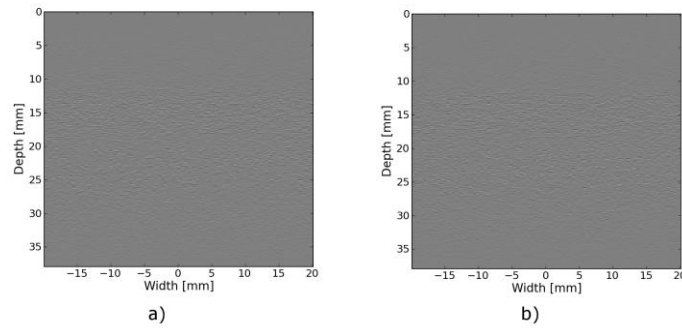


Figure 5.11: a) Pre-deformation and b) post-deformation ultrasound RF images. Motion tracking applied to these images generates the displacements in Fig. 5.12.

Displacements that define the motion between Fig. 5.11a) and Fig. 5.11b) are shown in Fig. 5.12. These images are created with the motion tracking algorithm described in Chapter 9. In the next few subsections, methods for calculating the displacement gradient from Fig. 5.12 are presented and the strain that results shown.

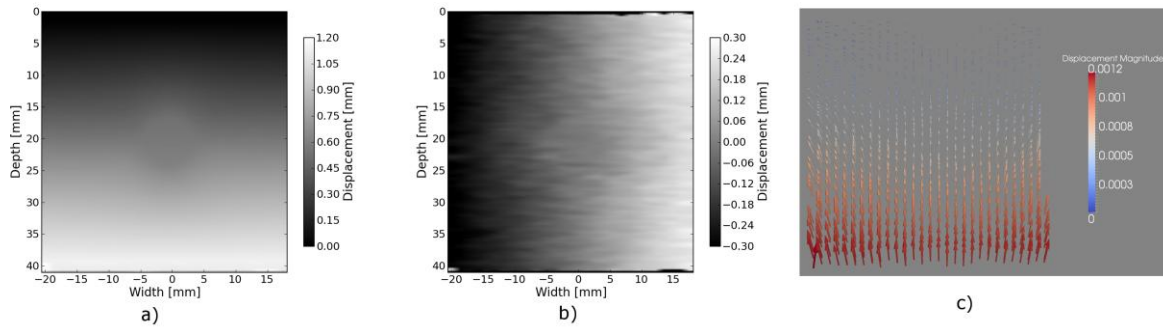


Figure 5.12: Displacements that result from tracking the motion in Fig. 5.11.

a) Axial displacements, b) lateral displacements, c) displacement vectors represented by arrows scaled and colored by their magnitude.

5.2.1 Finite difference based methods

A common way to approximate the first derivative of a function f at sample offset k using finite differences is the central difference method.

$$f'_0 \approx \frac{f_1 - f_{-1}}{2h}$$

Eqn. 5.37

where h is the sampling period.

This expression comes from a Taylor series expansion of the component terms

$$f_1 = f_0 + hf'_0 + \frac{h^2}{2!}f''_0 + \cdots + \frac{h^n}{n!}f^{(n)}_0 + \mathcal{O}(h^{n+1})$$

Eqn. 5.38

where $\mathcal{O}(h^{n+1})$ indicates the series has been truncated after $n+1$ terms.

We also have

$$f_{-1} = f_0 - hf_0^1 + \mathcal{O}(h^2)$$

Eqn. 5.39

Then we see

$$f_0^1 = \frac{f_1 - f_{-1}}{2h} + \mathcal{O}(h^2)$$

Eqn. 5.40

This approximation is, therefore, *second-order accurate*. Strain calculated using the central difference method to compute the displacement gradient is shown in Fig. 5.13.

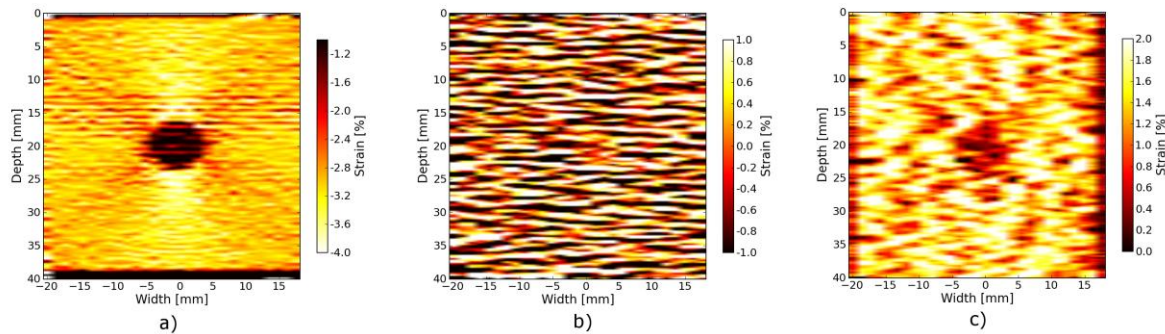


Figure 5.13: Strains calculated using the central difference method to compute the displacement gradient. a) Axial strain, b) shear strain, and c) lateral strain.

Other popular simple approaches for approximating the local derivative of sampled data include the forward difference method and the backward difference method. In the forward difference method,

$$f_0^1 \approx \frac{f_1 - f_0}{h}$$

Eqn. 5.41

After looking at the Taylor series expansion, the forward difference method, like the backward difference method, is first-order accurate.

$$f_0^1 = \frac{f_1 - f_0}{h} + \mathcal{O}(h)$$

Eqn. 5.42

Higher order accurate¹ approximations can be made by using additional samples. Various schemes will yield correct results as long as the Taylor series terms cancel. When there are equally spaced function samples, which are the most commonly encountered dataset and are the case for digital images, the coefficients are usually rational numbers because of the form of the Taylor series. For instance, a central difference approximation to the first derivative that uses a five point kernel is

$$f_0^1 = \frac{f_{-2} - 8f_{-1} + 8f_1 - f_2}{12h} + \mathcal{O}(h^4)$$

Eqn. 5.43

Khan and Ohba derived closed form expressions for higher order accurate approximations of

¹ Here we use the terminology *order of accuracy* to refer to the number of terms used in the Taylor series approximation and *order derivative* to refer to the degree of the derivative.

an arbitrary p^{th} order derivative [30, 31]. Two different sets of expressions were developed. The newer set of finite difference approximations uses samples from every other sample around the differentiated point. This set of approximations has the same computational complexity, and both approximations have linear phase and are highly accurate for polynomial type inputs [31]. However, these set of approximations have slightly better performance for periodic functions and functions sampled near the Nyquist frequency [31]. The second set of approximations is central difference type approximations that have symmetric non-zero coefficients for every point surrounding the sample of interest. The coefficients alternate in sign and decay rapidly from their center. The tap-coefficients, d , for a first order derivative are:

$$d_0 = 0$$

$$d_k = (-1)^{k+1} \frac{N!^2}{k(N-k)!(N+k)!}, \quad k = \pm 1, \pm 2, \dots, \pm N$$

Eqn. 5.44

The first sets of coefficients are explicitly given in Table 5.1.

Order of accuracy, 2N	Coefficients
2	-0.5, 0.0, 0.5
4	0.08333, -0.6667, 0.0, 0.6667, -0.08333
6	-0.016667, 0.15, -0.75, 0.0, 0.75, -0.15, 0.016667
8	0.00357143, -0.0380952, 0.2, -0.8, 0.0, 0.8, -0.2, 0.0380952, -0.00357143

10	-0.000793651, 0.00992063, -0.0595238, 0.238095, -0.238095, -0.833333, 0.0 0.833333, 0.0595238, -0.00992063, 0.000793651
----	--

Table 5.1: Tap-coefficients for higher order accurate center difference approximation of the first degree derivative.

Strain images with order of accuracy of 6 are displayed in Fig. 5.14.

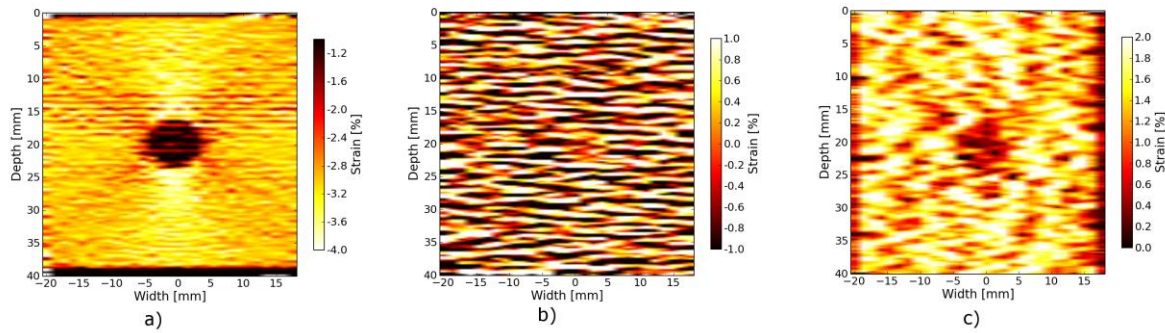


Figure 5.14: Cylindrical inclusion strain calculated with a 6th order-accurate central difference approximation. a) Axial strain, b) shear strain, and c) lateral strain.

Inspecting Fig. 5.13 and Fig. 5.14, only subtle differences are observed. There is noise present in Fig. 5.13 that remains present in Fig. 5.14. This noise is due not only to signal decorrelation but also artifacts related to the regularization described in Chapter 3. While the higher order-accurate calculation may be a more correct representation of the displacement gradients, it is sometimes primarily a more accurate representation of the noise present in the displacement gradients. In general some notable advantages have been observed. Specifically, there are reductions in the strain noise and an increase in the strain dynamic range. This behavior contrasts with the rest of the gradient calculation techniques discussed in this section, which tend to reduce the dynamic range resolution in the strain component images. Finite difference based methods are also among the most computationally efficient methods. They are

implemented as small, fast convolution kernels. However, they do little to filter out noise as the remaining techniques do.

5.2.2 Derivative of Gaussian

Convolution of an image with a Gaussian has a smoothing effect that removes high frequency content. In two dimensions, a Gaussian is given by

$$g(x_1, x_2) = \frac{1}{\sqrt{2\pi}\sigma} e^{-\frac{(x_1^2 + x_2^2)}{2\sigma^2}}$$

Eqn. 5.45

It follows from the derivative theorem and the convolution theorem, that convolving one function with the derivative of another is equivalent to taking the derivative of the first and convolving with the other [32].

$$(f * g)' = f' * g = f * g'$$

Eqn. 5.46

Thus, we can convolve the displacement images with a derivative of a Gaussian to get smoothed derivatives for the strain calculation. Since a large proportion of the high frequency content is often noise, this operation filters out noise. According to the derivative theorem, "If $f(x)$ has the Fourier transform $F(s)$, then $f'(x)$ has the Fourier transform $i2\pi sF(s)$. That is, the normal derivative operation, such as that achieved with finite difference operations, suppresses low frequency content and amplifies high frequency content since it is linear modulation. The derivative of a Gaussian can suppress the negative effects of amplification of high frequency

content. Results of convolution with a 2D Gaussian are found in Fig. 5.15.

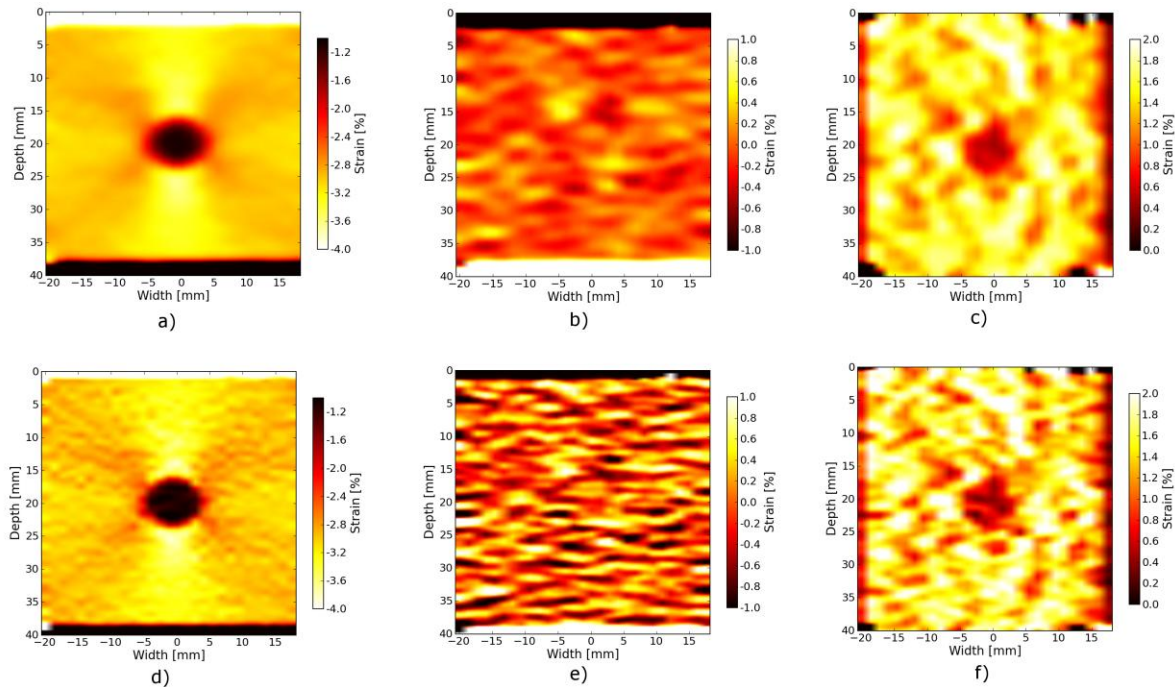


Figure 5.15: Strains from gradient calculation with the derivative of a 2D Gaussian having a-c) $\sigma = 1.0$ mm and d-f) $\sigma = 0.5$ mm.

The noise is reduced for both values of the smoothing parameter σ in Fig. 5.15a-c) and Fig. 5.15d-f). Of course, with too much smoothing, desired structural information also will be removed.

5.2.3 A modified least-squares strain estimator

An alternative approach to direct filtering out of the high frequency content is to fit the data with an approximating function of known form and use the derivative of the approximating function. This approach is taken in the next two subsections.

The least-squares strain estimator is simple, popular strain approximation method proposed by Kallel et al. [33]. A piecewise linear function is fit to the displacement data, and the slope of

this function is used in place of the derivative. To obtain the derivative of the displacement along direction 1, u_1 , with respect to direction x_1 , $\partial u_1 / \partial x_1$ around the datum $x_1^{(0)}$, first, the linear expression for a single datum is written,

$$u_1^{(0)} = m x_1^{(0)} + b$$

Eqn. 5.47

For a five point least-squares kernel in matrix form,

$$\begin{bmatrix} u_1^{(-2)} \\ u_1^{(-1)} \\ u_1^{(0)} \\ u_1^{(1)} \\ u_1^{(2)} \end{bmatrix} = \begin{bmatrix} x_1^{(-2)} & 1 \\ x_1^{(-1)} & 1 \\ x_1^{(0)} & 1 \\ x_1^{(1)} & 1 \\ x_1^{(2)} & 1 \end{bmatrix} \begin{bmatrix} m \\ b \end{bmatrix}$$

Eqn. 5.48

If this is written as,

$$\mathbf{u} = \mathbf{A} \begin{bmatrix} m \\ b \end{bmatrix}$$

Eqn. 5.49

Then the classic least-squares solution is [33, 34]

$$\begin{bmatrix} \hat{m} \\ \hat{b} \end{bmatrix} = (\mathbf{A}^T \mathbf{A})^{-1} \mathbf{A}^T \mathbf{u}$$

Eqn. 5.50

This can be written as

$$\begin{bmatrix} \hat{m} \\ \hat{b} \end{bmatrix} = \mathbf{A}^+ \mathbf{u}$$

Eqn. 5.51

where \mathbf{A}^+ is the Moore-Penrose pseudo-inverse of \mathbf{A} [34], which is found in practice using singular value decomposition. Note that if the spacing between displacement points is uniform along the direction of derivation, which it is for the displacement images, \mathbf{A}^+ will not change apart from handling boundaries, and it will only have to be found once for each direction of a displacement image that has unique spacing. The derivative is simply taken to be \hat{m} .

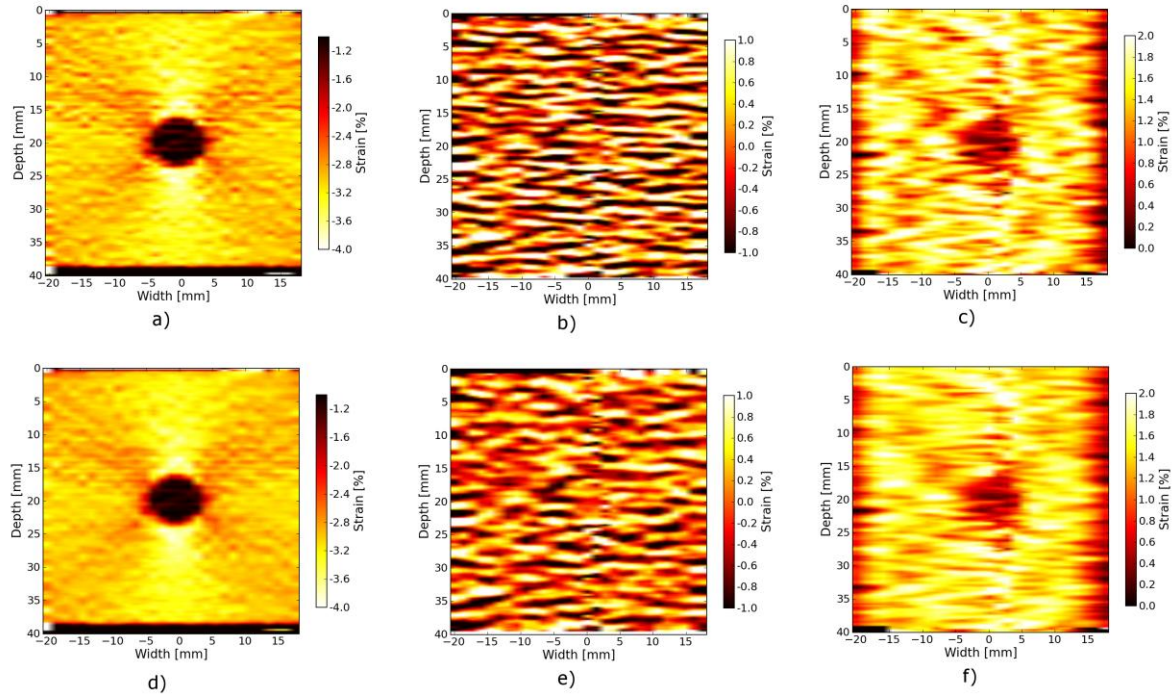


Figure 5.16: Strain images using local linear least-squares fit to the displacement data. a-c) 5 point least-squares kernel. d-f) 7 point least squares

kernel.

Results from the linear least-squares technique are shown in 5.16. Similar to the derivative of Gaussian results, high frequency noise is removed. Again, a longer kernel results in greater noise suppression but lower resolution.

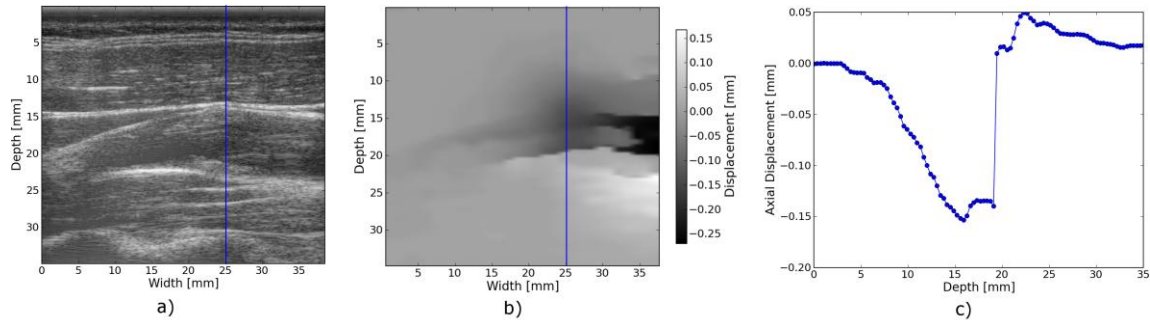


Figure 5.17: Longitudinal image the left carotid of subject 157. a) B-Mode, b) tracked axial displacements, c) line profile of the displacements in b) over the line overlaid on the images in a) and b). The motion is occurring during systole. Note the discontinuity of the displacement that occurs at the wall-lumen boundary around a depth of 20 mm.

In most tissues, such as breast tissue, the deformation is continuous and differentiable.

Deformation in the arteries, however, exhibits discontinuities in its motion. In a longitudinal view of the artery, Fig. 5.17, opposing arterial walls move in opposite directions. There is a discontinuity at the artery-lumen boundary. A motion tracking algorithm may follow the motion of blood or, more likely, signal in the area of the lumen that is from out-of-plane arterial tissue picked up by the wide elevational profile of the ultrasound beam. Alternatively, the motion tracking algorithm may track the motion of reverberations in the area of the lumen. In our experience, the tracked displacement is mostly continuous apart from the posterior wall-lumen boundary where divergence is recorded. This pattern is shown in Fig. 5.17b) and with greater detail in Fig. 5.17c). If the support of a derivative kernel operator passes over this discontinuity,

erroneous values will extend from the discontinuity almost the length of the kernel in both directions from the discontinuity.

To address this condition, the linear least-squares implementation can be modified. If the number of consecutive displacement samples with the same sign exceeds half the width of the kernel, only these samples can be used in the linear least-squares fit. In this way, values from only one side or the other of the discontinuity are used for the local gradient estimate. Axial strain results of this modified least-squares method applied to the carotid artery are shown in Fig. 5.18. The effects of the discontinuity are greatly reduced without affecting other parts of the image. Correctly estimating the strain in this area is important since we are most interested in the strain in the vessel wall. Note that is still a small positive streak at the vessel-wall border. Close inspection reveals that this streak is primarily within the lumen. Its source can be observed in Fig. 5.17c) in the segment following the sharp discontinuity. It is possibly explained by the finite match-block kernel length or possibly the way the regularization algorithm (Chapter 3) encourages continuity.

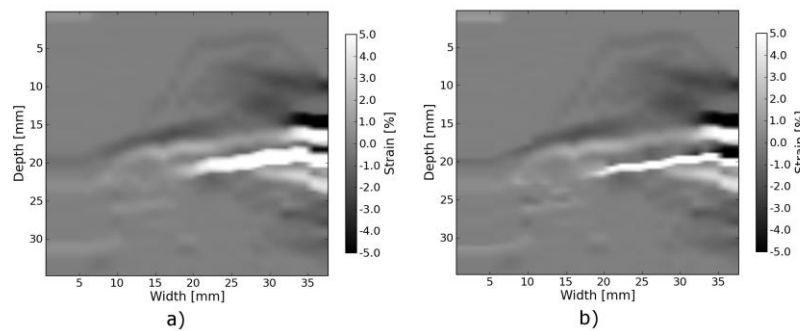


Figure 5.18: Axial strain in the vessel show in Fig. 5.17. a) Strain calculated with the standard linear least-squares method. b) Strain calculated with the modified linear least-squares method described in the text.

5.2.4 B-spline fitting

Instead of approximating the displacement field with a piecewise linear function, the displacement field can be approximated with piecewise continuous spline fitting. This function is more appealing than a piecewise linear fit for several reasons. First, the splines are constructed to be piecewise continuous [35, 36]. Second, if a B-spline is used, the first derivative will be continuous if the order of the spline is two or higher [35, 36]. Third, the greater flexibility of higher order polynomials should decrease the loss in resolution observed with the linear least-squares strain estimator [37]. Khadem and Setarehdan applied this method in 1D to determine axial strains [37]. A piecewise continuous polynomial spline was fit to the discrete noisy displacement data, and the derivative of the resulting polynomial was used as the derivative of the underlying displacement [37]. D'hooge et al. performed a similar procedure with a cubic B-spline approximation to track M-Mode data to obtain strain rates in a gelatin phantom [38]. In both articles, the spline did not interpolate the underlying displacement data, but it was fit by minimizing a term involving the squared difference with the sampled data and another regularization term involving the square of the second derivative of the underlying function. Applying a higher weight to the later term will increase the smoothness of the result.

In what follows, a least-squares 2D cubic B-spline approximation based on the work of Tustison et al. is applied to the displacement data [39]. Once the fit is performed, the gradient of the resulting function can be found analytically anywhere in the image domain. The method is parameterized by the number of B-spline control points. In the results presented in Fig. 5.19, control point density is expressed as the ratio of control point spacing to the displacement sample spacing.

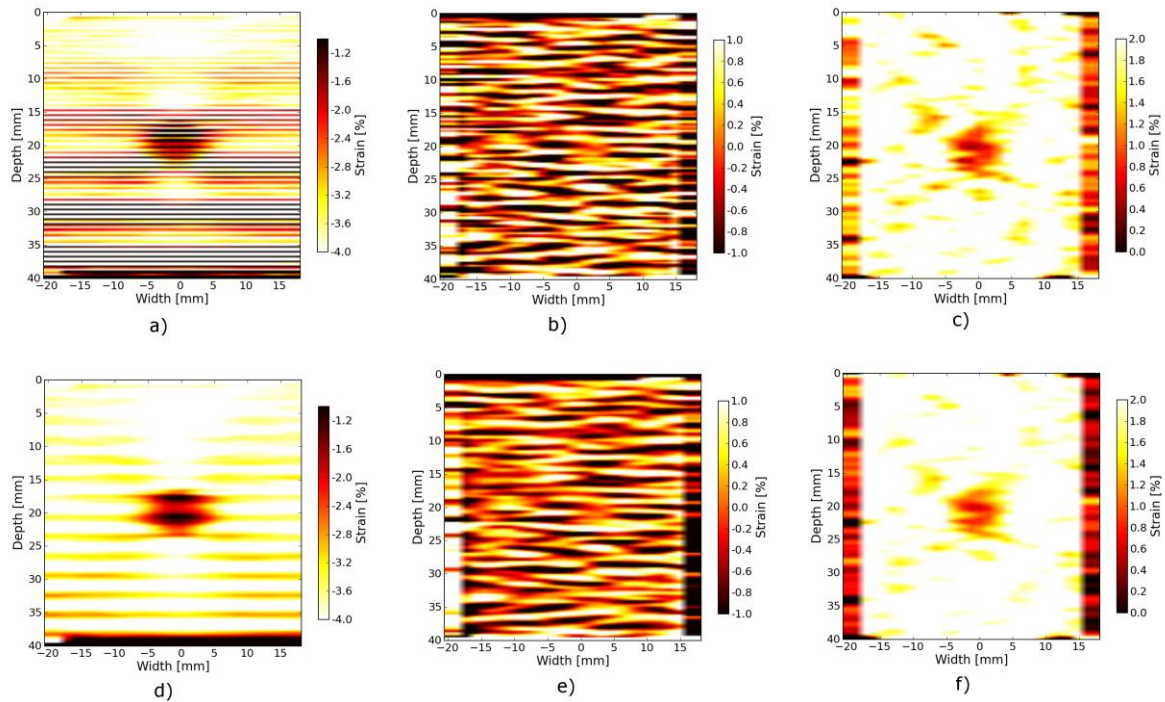


Figure 5.19: Strains resulting from the cylindrical inclusion model using a cubic B-spline least squares fit to calculate the displacement gradient. a-c) control point spacing to displacement sample spacing ratio of 1.5. d-f) control point spacing to displacement sample spacing ratio of 1.8.

While smoothing is present in Fig. 5.19, there are also very noticeable and unacceptable oscillation artifacts. The artifacts are greatest in the axial strain images. When the control point spacing is increased, the frequency of the artifacts decreases. The presence of these artifacts can be explained by two sources. A numerical insufficiency in the current implementation of the regularization method described in Chapter 3 causes bias toward integer sample displacements. The higher order polynomial function fit exaggerates this bias and causes extensive oscillations. Runge's phenomenon [40] states that higher order polynomial fitting functions may actually result in poorer performance because of the oscillations that result. This can be attributed to the increased extrema ($n-1$ for a polynomial of order n) that are required with increasing polynomial

orders. In order for B-spline fitting to be successful in this algorithm, a few actions could be taken. First, the bias artifacts could be reduced or eliminated with a re-implementation of the regularization algorithm. Also, smoothness of the B-spline could be enforced by adding a regularization term to the fit that penalizes the presence of the $L2$ norm of the second derivative.

5.3 Useful quantities derived from the strain tensor

5.3.1 Principal strains

Since strain is a tensor instead of a scalar, it is not rotation invariant. Consequently, for the same tissue deformation, the axial strain in a certain volume of tissue will change depending on the orientation of the beam axis relative to the tissue. When a tensor is subject to a linear transformation, such as a rotation, the transformed tensor is given by [1],

$$[\mathbf{Q}]^T [\mathbf{T}] [\mathbf{Q}]$$

Eqn. 5.52

where \mathbf{Q} is the transformation on the tensor \mathbf{T} . There is a particular rotation of the strain tensor \mathbf{E} that provides a more transparent interpretation of the tensor.

Recall that when

$$\mathbf{E}\mathbf{n} = \lambda\mathbf{n}$$

Eqn. 5.53

if \mathbf{E} is a tensor, \mathbf{n} is a vector, and λ is a scalar, \mathbf{n} is called an eigenvector of \mathbf{E} , and λ is an eigenvalue of \mathbf{E} . Basic linear algebra states that every real, symmetric tensor will have

eigenvalues and corresponding eigenvectors that are mutually perpendicular [1]. Since the strain tensor is a real, symmetric tensor, it has eigenvalues and eigenvectors. If unit length eigenvectors are used as the columns of a transformation matrix for the associated tensor, the transformed result will be a diagonal matrix whose entries are the eigenvalues. The eigenvalues of \mathbf{E} are called the *principal strains* of \mathbf{E} , and the eigenvectors of \mathbf{E} are called the *principal directions* of \mathbf{E} [1].

Rotating a tensor is equivalent to looking at the tensor in a different coordinate system orientation. With this in mind, the principal directions define the most convenient orientation to view a strain tensor. The principal strains have the largest possible magnitude of normal strain. No shear strains are present.

5.3.2 Representation of the 2D strain tensor as an ellipse

In section 5.1, it was shown that a strain tensor describes the change in relationship between two small vectors in a body. Second-rank tensors in general are characterized by how they modify these two vectors.

Another second-rank tensor of importance in medical imaging is the diffusion tensor. This tissue property has proven to be a useful tool for exploring neural physiology and pathology with MRI. Diffusion of water molecules can cause a decay in the received echo amplitude because of their displacement in the spatially varying magnetic-field gradient, which is given by [41]

$$\ln \left[\frac{A(TE)}{A(0)} \right] = -\gamma^2 \left[\delta^2 \left(\Delta - \frac{\delta}{3} \right) + \frac{\varepsilon^3}{30} - \frac{\delta^2}{\varepsilon} 6 \right] \mathbf{g}^T \mathbf{D} \mathbf{g}$$

Eqn. 5.54

where $A(TE)$ is the amplitude of the magnetization at the time of the echo,

$\gamma^2 \left[\delta^2 \left(\Delta - \frac{\delta}{3} \right) + \frac{\varepsilon^3}{30} - \frac{\delta^2}{\varepsilon} 6 \right]$ are a set of pulse sequence parameters, \mathbf{g} is the vector of the magnetic-field gradients, and \mathbf{D} is the diffusion tensor. Like the strain tensor, the diffusion tensor is symmetric and real, so it has eigenvalues, λ_i , and eigenvectors [42]. The eigenvectors are the principal diffusivity directions and the eigenvalues are the principal diffusivities [42]. The largest principal diffusivity can identify neural tissue's fiber track direction as the principal direction associated with that eigenvalue [43, 42].

The probability density function that a molecule diffuses from location \mathbf{x}_0 to position \mathbf{x} at time τ is given by [42],

$$\rho(\mathbf{x}|\mathbf{x}_0, \tau) = \frac{1}{\sqrt{|\mathbf{D}(\tau)|(4\pi\tau)^3}} \exp \left[\frac{-(\mathbf{x} - \mathbf{x}_0)^T \mathbf{D}^{-1}(\tau) (\mathbf{x} - \mathbf{x}_0)}{4\tau} \right]$$

Eqn. 5.55

The probability of displacement of a molecule is dependent on the inverse of the diffusion tensor, whose eigenvectors are the same as \mathbf{D} and whose eigenvalues are $1/\lambda_i$. If the inverse diffusion tensor is applied in a quadric operation on the vector \mathbf{x} and set equal to a constant, the expression represents the relative diffusivity in direction \mathbf{x} [42]. If the matrix has been diagonalized, the expression has the form,

$$\frac{x_1^2}{\lambda_1^2} + \frac{x_2^2}{\lambda_2^2} + \frac{x_3^2}{\lambda_3^2} = 1$$

Eqn. 5.56

This expression describes an ellipsoid with λ_1 , λ_2 , and λ_3 , being the lengths of the principal axes [44]. The ellipsoid represents the diffusivity in any given direction, \mathbf{x} .

As discussed in the derivation of the strain tensor in Section 5.1.1, the quadric operation of the strain tensor on a differential line segment in a body effectively relates the stretching or compression of that segment. As with the diffusion tensor, the strain tensor can be visualized as an ellipse in 2D or an ellipsoid in 3D [45, 44]. This representation is called a *Lamé ellipsoid* [45].

Note that this geometrical representation does not always strictly follow from the strain tensor. The diffusion tensor is positive definite [42]; therefore, its determinant is always positive and its eigenvalues are always positive. This is not true for the strain tensor; the principal strains can be positive (stretching) or negative (compression). In fact, due to the Poisson effect [46], stretching of a material in one direction often causes stresses that drive compressions in the orthogonal directions, and the signs of the principal strains are usually varied. In 2D, if one of the principal strains is negative, the expression is no longer represented by an ellipse but by a hyperbola,

$$\frac{x_1^2}{\lambda_1^2} - \frac{x_2^2}{\lambda_2^2} = 1$$

Eqn. 5.57

In 3D, if one of the principal strains is negative the quadratic expression specifies a hyperboloid of one sheet, and if two of the principal strains are negative, then the quadric surface is a hyperboloid of two sheets [44]. Unfortunately, hyperboloids are not closed surfaces, and it is difficult to visualize it as a glyph. Therefore, the strain is represented as an ellipse or ellipsoid

where the lengths of the principal axes are the absolute value of the principal strains, and the orientation of the ellipse is specified by the principal directions. An interpretation of the ellipse is therefore the stretching or compression that occurs in a given direction. Visualization of the noiseless strain tensor image for a cylindrical inclusion undergoing uniaxial compression (examined in Section 5.2) is shown in Fig. 5.20.

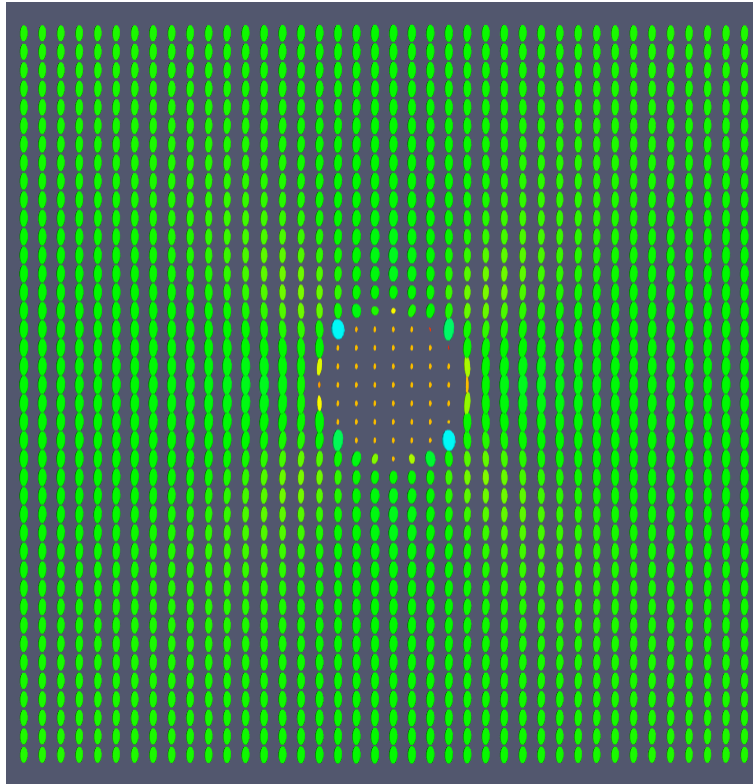


Figure 5.20: Visualization of the strain tensor field for a cylindrical inclusion undergoing uniaxial compression.

5.3.3 Combination of normal strains and shear strain into a single strain index

It is easier to perform statistical hypothesis testing with a single, scalar strain statistic than with the full second-order tensor. With the appropriate scalar quantity derived from the tensor, comparisons can be made to other metrics that quantify plaque vulnerability, and a number that

indexes likelihood of plaque rupture will hopefully be obtained. The three strain tensor components estimated from a 2D image can be combined into a single strain index using metrics developed in the field of material plasticity theory. In material plasticity theory, a yield criteria prescribes the point a deformed material will no longer return to its original state after the load is removed [46]. Yield criteria that have been studied for engineering materials include the maximum principal strain, the maximum shear stress (Tresca yield criteria), the total strain energy, or the distortion energy (von Mises yield criteria) [46]. These criteria compare a single index to a material dependent threshold that determines the transition point from elastic (recoverable) to plastic (non-recoverable) deformation. They are most often given in stress form, but here their 2D strain analogs are used with our 2D strain tensor imaging algorithm data. For example, given λ_1 and λ_2 , the ordered principal strains, strain metrics to examine include the maximum principal strain,

$$\max \{|\lambda_1|, |\lambda_2|\}$$

Eqn. 5.58

the maximum shear strain,

$$\lambda_1 - \lambda_2$$

Eqn. 5.59

total strain energy,

$$\frac{1}{2}E (\lambda_1^2 + \lambda_2^2)$$

Eqn. 5.60

and the distortional energy,

$$\frac{1}{2}E (\lambda_1 - \lambda_2)^2$$

Eqn. 5.61

The latter has been used by Maurice et al. for the examination of carotid plaque [47]. Note that although the modulus, E , is unknown, plaque materials that have a low E generally possess a low ultimate failure strain [48]. Thus, a plaque region with a high energy metric is likely near the failure strain if it has a high modulus and high failure strain or if it has a low modulus and low failure strain. In other words, since E is unknown, the 'total strain energy' and 'distortional energy' calculated is only proportional to these quantities. However, this may be sufficient because of the material properties of the plaque constituents.

5.4 Generating accumulated strain from a time series

5.4.1 Dynamic frame skip

As seen in the elastographic signal-to-noise ratio ($SNRe$) results in Chapter 3, Fig. 3.3, and Chapter 4, Fig. 4.1, the ability for an algorithm to achieve a good strain image signal-to-noise ratio depends on the magnitude of the strain. This was explored theoretically and experimentally by Varghese et al. [49]. If the amount of deformation in the image is too low, electronic and

quantization noise prevent determination of the motion in the image with precision [49]. If the deformation is too high, the image pair will decorrelate [49].

When data is collected *in vivo*, a series of image frames are collected. To obtain high quality motion tracking, frame pairs should be chosen that have the amount of deformation that will yield the highest quality results. Motion tracking does not need to occur between consecutive frames. The most appropriate frame skip between the pre-deformation image and the post-deformation image should be chosen.

When the mechanical load on the tissues being imaged comes from cardiac pulsations, the strain rate in an image sequence is non-constant. A higher strain rate occurs during systole, and a lower strain rate occurs at end diastole. To retain optimal tracking over a sequence of images spanning the cardiac cycle, a dynamic frame skip is applied that uses a short frame skip when the strain rate is high, and a long frame skip with strain rate is slow.

To apply an automatic method that ascertains an ideal frame skip, the optimal deformation must be defined in a quantifiable way. This is application specific. For example, when the objective is to get a strain image of a breast tissue abnormality, the frame average strain may be a good measure. When imaging carotid plaques, we are only interested in the strain inside the plaque. There is relatively little deformation in the skin and muscle near the transducer, but the deformation in these areas should not determine the frame skip. Also, there may be apparently high strain in the region of the lumen, but tracking in this area is unreliable. The criteria that determines the frame skip in this work is based on the axial strain in a sub-region of the image. The top and bottom portions are removed from the region-of-interest (ROI) because the skin and fat near the transducer are not the target tissue of interest and because attenuation decreases signal quality at depths beyond the vessel. The frame skip is dynamically increased or decreased

based on an absolute ROI axial strain threshold. Peak-hopping errors generally are also undesirable, which will present as unrealistically high strains. Peak-hopping is acceptable in the lumen, however, so an additional frame skip criteria is percent axial strain pixels in the ROI over a threshold.

When it is time to track the next frame pair in a sequence, the previous frame skip is initially attempted. If both criteria are below threshold, the frame skip is increased until they exceed threshold, and the prior tracking result is used. An exception to the prior behavior is a halt to the increase in the frame skip if the magnitude of the strain decreases, which could occur during the transition from systole to diastole or at the dichrotic notch. On the other hand, if either criteria are above threshold, the frame skip is decreased until they are below threshold.

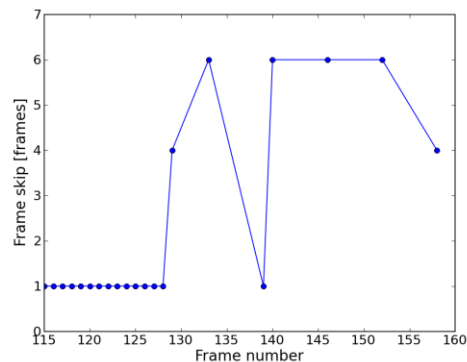


Figure 5.21: Frame skip for tracking of subject 157's left carotid over the period of a single cardiac cycle. A small frame skip is used during systole when the strain rate is high, and a larger frame skip is used during diastole when the strain rate is small. The maximum frame skip was limited to six frames.

For the purposes of creating a video to view the tracked results, it is more convenient to have the displacement and strain images available at regular time steps. Standard video encoding and decoding software assume a constant frame rate. If a dynamic frame skip is used,

displacement images must be interpolated at the shortest period between tracked frames.

Incremental displacement images are interpolated to the original frame rate with the following algorithm:

1. Set a frame counter i to 1.
2. Calculate the fraction of displacement remaining, p , as $(n-i)/(n-i+1)$, where n is the frame skip.
3. The output displacement for the current frame is $(1-p)$ multiplied by the remaining displacement.
4. This remaining displacement is multiplied by p .
5. A correction field is calculated the inverse of the prior frame displacement.
6. Warp the remaining displacement by the correction field.
7. Increment i and repeat at step 2. until $i = n$.

This process is non-trivial because the displacement image is defined on a grid with uniform spacing. The inverse displacement field is calculated with the algorithm given by Chen et al. [50].

5.4.2 Eulerian approach to accumulated strain

Since strain is a measure of the distortion of an object relative to a reference strain, the *reference state* must be defined. Experimentalists whom attempt to measure the *in vitro* mechanical properties will sometimes try to find a complete stress-free state of the artery and use this as the reference state. When removed from the tethering provided by surrounding tissue, arteries will shrink dramatically in size [51]. A *no-load* [51] condition occurs when excised vessels are removed and blood pressure and longitudinal tensile stresses are removed. A *zero stress* [51] occurs when no further strain occurs after cutting the tissue. The residual stress that defines the difference between the no-load and zero stress can be quantified with the opening angle, the angle that results from cutting an artery longitudinally [51]. When working with *in vivo* tissues, it is difficult to infer the zero stress state, although Masson et al. obtained reasonable results given a number of modeling assumptions for a healthy common carotid artery [52]. For

this reason, an end diastolic image state is taken as the reference state.

To get the strain that occurs over a cardiac cycle, the deformations calculated with the dynamic frame skip tracking must be accumulated. Since the strains observed in a cardiac cycle are typically large, > 0.05 , accumulating infinitesimal strain (Section 5.1.1.1) is inappropriate. Since the displacements are calculated incrementally, the reference material is always changing, and Eulerian-Almansi strain tensor should be accumulated because it consistently specifies strain in terms of the spatial configuration [2].

Two additional factors make calculation of the accumulated strain non-trivial. First, the displacement and strain fields are discretely sampled and saved as digital data. Secondly, the plaque moves in its location with the image over the cardiac cycle. To address these challenges, a particle method is applied to the purpose of finding the accumulated strain. First the plaque ROI is segmented by a radiologist at end-diastole with the medical interaction toolkit (MITK) [53]. This creates a binary label image. All the points in the binary image labeled as plaque are used to create a quadrilateral mesh. Accumulated strain and accumulated displacement is then calculated over the points in the mesh. For every frame, the mesh is first warped by the incremental displacement by translating coordinates of the points in the mesh. This translation is determined via bilinear interpolation of the incremental displacement vector image. The incremental strain or incremental displacement for each point in the mesh is found with bilinear interpolation and added to the accumulated strain or accumulated displacement for that point (particle). This process is repeated for every frame. Since coordinates of particles in the mesh are recorded as real numbers, this system handles subpixel displacements well. Note that the mesh is warped prior to adding the incremental strain for a given frame because we are using Eulerian-Almansi strain instead of Green-Lagrangian strain.

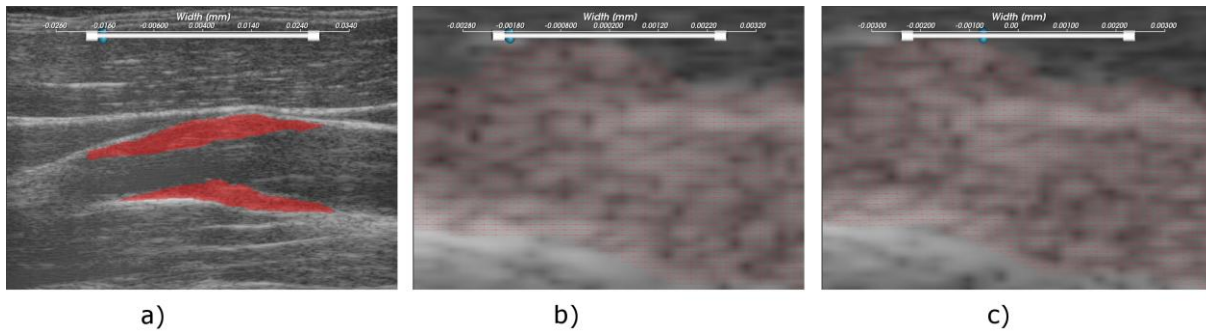


Figure 5.22: Mesh warping for subject 157. a) Segmented plaque in the longitudinal view. b) A mesh of particles is created from the segmented ROI. c) The mesh is warped by the incremental tracked displacements.

5.5 References

- [1] W. M. Lai, D. Rubin and E. Kreml. *Introduction to Continuum Mechanics*. : Elsevier. 1993.
- [2] P. Haupt. *Continuum Mechanics and Theory of Materials*. New York: Springer. 2002.
- [3] J. Rogowska. Optical coherence tomographic elastography technique for measuring deformation and strain of atherosclerotic tissues. *Heart* 90, 556--562. 2004.
- [4] J. Rogowska, N. Patel, S. Plummer and M. E. Brezinski. Quantitative optical coherence tomographic elastography: method for assessing arterial mechanical properties. *The British Journal of Radiology* 79, 707--11. 2006.
- [5] D. Stamper, N. J. Weissman and M. Brezinski. Plaque characterization with optical coherence tomography. *Journal of the American College of Cardiology* 47, C69--79. 2006.
- [6] R. Chan, A. Chau, W. Karl, S. Nadkarni, A. Khalil, N. Iftimia, M. Shishkov, G. Tearney, M. Kaazempur-Mofrad and B. Bouma. OCT-based arterial elastography: robust estimation exploiting tissue biomechanics. *Optics Express* 12, 4558--72. 2004.
- [7] B. H. Han, M. H. Cho and S. Y. Lee. "Strain mapping by Image Correlation For X-Ray Elastography". In (Eds.) *Ninth International Conference on the Ultrasonic Measurement and Imaging of Tissue Elasticity*, : . 2010.
- [8] J. Fowlkes, S. Emelianov, J. Pipe, A. Skovoroda, P. Carson, R. Adler and A. Sarvazyan. Magnetic-resonance imaging techniques for detection of elasticity variation. *Medical Physics* 22, 1771. 1995.
- [9] J. Bishop, G. Poole, M. Leitch and D. B. Plewes. Magnetic resonance imaging of shear wave propagation in excised tissue. *Journal of Magnetic Resonance Imaging* 8, 1257--65. 1995.
- [10] P. Hardy. Imaging articular cartilage under compression--cartilage elastography. *Magnetic Resonance in Medicine* 53, 1065--73. 2005.
- [11] D. B. Plewes, J. Bishop, A. Samani and J. Sciarretta. Visualization and quantification of breast cancer biomechanical properties with magnetic resonance elastography. *Physics in Medicine and Biology* 45, 1591. 2000.
- [12] E. B. A. P. Lin. Circumferential strain in the wall of the common carotid artery: Comparing displacement-encoded and cine MRI in volunteers. *Magnetic Resonance in Medicine* 60, 8--13. 2008.
- [13] G. Korosoglou and A. Youssef. Real-time fast strain-encoded magnetic resonance imaging to evaluate regional myocardial function at 3.0 Tesla: comparison to conventional tagging. *Journal of Magnetic Resonance Imaging* 27, 1012--8. 2008.
- [14] M. Neizel, D. Lossnitzer, G. Korosoglou, T. Sch"aufele, A. Lewien, H. Steen and H. Katus. Strain-encoded (SENC) magnetic resonance imaging to evaluate regional heterogeneity of myocardial strain in healthy volunteers: Comparison with conventional tagging. *Journal of Magnetic Resonance Imaging* 29, 99--105. 2009.
- [15] M. L. Shehata and T. Basha. Real-time single-heartbeat fast strain-encoded imaging of right ventricular regional function: normal versus chronic pulmonary hypertension. *Magnetic*

Resonance in Medicine 64, 98--106. 2010.

[16] J. Ophir, F. Kallel, T. Varghese, E. Konofagou, S. K. S. K. Alam, T. Krouskop, B. Garra and R. Righetti. Elastography. *Comptes Rendus de l'Academie des Sciences - Series IV - Physics* 2, 1193--1212. 2001.

[17] J. Ophir, B. Garra, F. Kallel, E. Konofagou, T. Krouskop, R. Righetti and T. Varghese. Elastographic imaging. *Ultrasound in Medicine and Biology* 26, S23----S29. 2000.

[18] K. Parker, L. Gao, R. Lerner and S. Levinson. Techniques for elastic imaging: a review. *IEEE Engineering in Medicine and Biology Magazine* 15, 52--59. 1996.

[19] K. J. Parker, M. M. Doyley and D. J. Rubens. Imaging the elastic properties of tissue: the 20 year perspective. *Physics in Medicine and Biology* 56, R1--R29. 2011.

[20] J. Ophir, I. Cespedes, H. Ponnekanti, Y. Yazdi and X. Li. Elastography: a quantitative method for imaging the elasticity of biological tissues. *Ultrasonic Imaging* 13, 111--134. 1991.

[21] H. H. G. Hansen, R. G. P. Lopata, T. Idzenga and C. L. de Korte. Full 2D displacement vector and strain tensor estimation for superficial tissue using beam-steered ultrasound imaging.. *Physics in Medicine and Biology* 55, 3201--18. 2010.

[22] A. Thitaikumar, L. M. Mobbs, C. M. Kraemer-Chant, B. S. Garra and J. Ophir. Breast tumor classification using axial shear strain elastography: a feasibility study. *Physics in Medicine and Biology* 53, 4809--23. 2008.

[23] I. O. Wygant, X. Zhuang, D. T. Yeh, O. Oralkan, A. Sanli Ergun, M. Karaman and B. T. Khuri-Yakub. Integration of 2D CMUT arrays with front-end electronics for volumetric ultrasound imaging. *IEEE Transactions on Ultrasonics, Ferroelectrics, and Frequency Control* 55, 327--42. 2008.

[24] Mart. 2D array design based on Fermat spiral for ultrasound imaging. *Ultrasonics* 50, 280--9. 2010.

[25] B. Byram, G. Holley, D. Giannantonio and G. Trahey. 3-D phantom and in vivo cardiac speckle tracking using a matrix array and raw echo data. *IEEE Transactions on Ultrasonics, Ferroelectrics, and Frequency Control* 57, 839--54. 2010.

[26] M. J. Po, A. Lorsakul, Q. Duan, K. J. Yeroushalmi, E. Hyodo, Y. Oe, S. Homma and A. F. Laine. "In-vivo clinical validation of cardiac deformation and strain measurements from 4D ultrasound". In (Eds.) *IEEE Engineering in Medicine and Biology Society*, : IEEE. 2010.

[27] R. Lopata, M. Nillesen, I. Gerrits, J. Thijssen, L. Kapusta and C. de Korte. "4D cardiac strain imaging: methods and initial results". In (Eds.) *Proc. IEEE Ultrasonics Symp*, : Ieee. 2007.

[28] M. Rao and T. Varghese. Correlation analysis of three-dimensional strain imaging using ultrasound two-dimensional array transducers. *The Journal of the Acoustical Society of America* 124, 1858--65. 2008.

[29] T. G. Fisher, T. J. Hall, S. Panda, M. S. Richards, P. E. Barbone, J. Jiang, J. Resnick and S. Barnes. Volumetric elasticity imaging with a 2-D CMUT array.. *Ultrasound in Medicine & Biology* 36, 978--90. 2010.

[30] I. Khan and R. Ohba. Closed-form expressions for the finite difference approximations

of first and higher derivatives based on Taylor series. *Journal of Computational and Applied Mathematics* 107, 179--193. 1999.

[31] I. Khan and R. Ohba. Taylor series based finite difference approximations of higher-degree derivatives. *Journal of Computational and Applied Mathematics* 154, 115 -- 124. 2003.

[32] R. N. Bracewell. *The Fourier Transform and Its Applications*. : McGraw-Hill. 2000.

[33] F. Kallel and J. Ophir. A least-squares strain estimator for elastography. *Ultrasonic Imaging* 19, 195--208. 1997.

[34] W. Weisstein, Eric. Moore-Penrose Matrix Inverse. From MathWorld-- A Wolfram Web Resource. 2011. <http://mathworld.wolfram.com/Moore-PenroseMatrixInverse.html>.

[35] W. Boehm. Bezier- and B-spline techniques. **, . 2002.

[36] L. A. Schwarz. Non-rigid Registration Using Free-form Deformations. 2007.

[37] A. Khadem and S. K. Setarehdan. Smoothing-spline Based Strain Estimation in Ultrasound Elastography. *Simulation* 00, 24--27. 2007.

[38] J. D'hooge, P. Claus, B. Bijmens, J. Thoen, F. Van de Werf, G. R. Sutherland and P. Suetens. Robust strain rate estimation using two-dimensional cubic B-splines. *2002 IEEE Ultrasonics Symposium, 2002. Proceedings.* 00, 1881--1884. 2002.

[39] N. J. Tustison and J. C. Gee. ND \$ Cbackslash^ k \$ B-Spline Scattered Data Approximation. *The Insight Journal* 2, . 2005.

[40] C. Maes. Runge's Phenomenon. Wolfram Demonstrations Project. 2011. <http://demonstrations.wolfram.com/RungesPhenomenon/>.

[41] P. Basser, J. Mattiello and D. Lebihan. Estimation of the effective self-diffusion tensor from the NMR spin echo. *Journal of Magnetic Resonance Series B* 103, 247--247. 1994.

[42] P. Basser. MR diffusion tensor spectroscopy and imaging. *Biophysical Journal* 66, 259--267. 1994.

[43] C. Pierpaoli and P. J. Basser. Toward a Quantitative Assessment of Diffusion Anisotropy. *Magnetic Resonance in Medicine* 36, 893--906. 1996.

[44] J. Roe. *Elementary Geometry*. New York: Oxford University Press. 1993.

[45] D. Sosa-Cabrera, K. Krissian, J. Gonzalez-Fernandez, L. Gomez-Deniz, E. Rovaris, C. Casta~no-Moraga and J. Ruiz-Alzola. Strain Tensor Elastography: 2D and 3D Visualizations. 2009.

[46] L. S. Srinath. *Advanced Mechanics of Solids*. : McGraw-Hill. 2003.

[47] R. L. Maurice, J. Ohayon, G. Finet and G. Cloutier. Adapting the Lagrangian speckle model estimator for endovascular elastography: Theory and validation with simulated radio-frequency data. *Journal of the Acoustical Society of America* 116, 1276--1286. 2004.

[48] G. A. Holzapfel, G. Sommer and P. Regitnig. Anisotropic mechanical properties of tissue components in human atherosclerotic plaques. *Journal of Biomechanical Engineering-Transactions of the ASME* 126, 657--665. 2004.

[49] T. Varghese and J. Ophir. A theoretical framework for performance characterization of elastography: the strain filter. *IEEE Transactions on Ultrasonics, Ferroelectrics, and Frequency*

Control 44, 164--72. 1997.

[50] M. Chen, W. Lu, Q. Chen, K. J. Ruchala and G. H. Olivera. A simple fixed-point approach to invert a deformation field. *Medical Physics* 35, 81. 2008.

[51] Y. Fung. *Biomechanics: mechanical properties of living tissues*. : Springer. 1993.

[52] I. Masson, P. Boutouyrie, S. Laurent, J. D. Humphrey and M. Zidi. Characterization of arterial wall mechanical behavior and stresses from human clinical data. *Journal of Biomechanics* 41, 2618--27. 2008.

[53] D. Maleike, M. Nolden, H. Meinzer and I. Wolf. Interactive segmentation framework of the Medical Imaging Interaction Toolkit. *Computer Methods and Programs in Biomedicine* 96, 72--83. 2009.